Turbulent Flow Structures around a Wavy Square Cylinder Based on Large Eddy Simulation

Dan Zhang[a], Akira Rinoshika[b], Yan Zheng[a],*,**, Zijuan Li[a], and Ya Zhang[a]

[a] *School of Automotive and Traffic Engineering, Jiangsu University of Technology, Changzhou, Jiangsu, China*
[b] *Department of Mechanical Systems Engineering, Graduate School of Science and Engineering Yamagata University, Yamagata, Japan*
*e-mail: zy30003333@163.com
**e-mail: zhengyan@jsut.edu.cn

Abstract—Flow structures around a wavy square cylinder with a perturbation wavelength of $5.6D$ are investigated using large eddy simulation at the Reynolds number of 23 500. The detailed force characteristics and wake flow structures of the wavy square cylinder are captured and compared with a square cylinder. Under the effect of wavy leading edge up to 27% and 98% reduction in the mean drag and the lift fluctuations are achieved, respectively. The 3D mean flow field implies a high shear flow between node and saddle positions, which is associated with the generation of additional streamwise and vertical vortex pairs. These vortex structures are responsible for the three-dimensionality of the wake flow behind the wavy square cylinder. The instantaneous flow patterns suggest that the staggered pattern of von Kármán vortex shedding is suppressed and replaced by symmetric vortex shedding into the near wake region of the wavy square cylinder. This symmetric vortex structure in the near wake plays a role in preventing the upper and lower shear layers from interacting with each other. The time—frequency analysis exhibits a reduction in the dominating vortex shedding frequency for the case of wavy square cylinder, indicating a relatively steady wake flow. This can be attributed to the vortex dislocation behind the wavy square cylinder. In the range of high frequencies, small streaks associated with small-scale fluctuations are enhanced by the wavy leading edge. The present study suggests that the perturbation wavelength obtained from the wavelength of Mode A instability at laminar flow regime can be served as a basis for flow control in turbulent flow regime.

Keywords: wake, vortices, time-frequency analysis, square cylinder

DOI: 10.1134/S0015462822010116

Turbulent flows past bluff bodies occur frequently in many engineering applications, such as heat exchangers, chimneys, high-rise buildings, and bridge decks. The common features of flow around bluff bodies involve the formation of turbulence and the transport of vortices. These features can be associated with drag force, lift fluctuations, flow-induced vibration (FIV), and acoustic noise of bluff bodies. In the past two decades, various flow control strategies have been developed to mitigate these adverse effects by modifying the flow field around bluff bodies [1—5]. To implement an efficient flow control, the understanding and anticipation of the properties of flow around bluff bodies are significantly important.

Owing to the development of knowledge on three-dimensionality of various bluff bodies [6—11], it has been well-established that the near wake of a two-dimensional bluff body is dominated by two kinds of instabilities. The dominating primary instability is responsible for the formation of vortex street, while the secondary instabilities are associated with the three-dimensional wake transition. These secondary instabilities promote the development of the shear-layer three-dimensionality and divert the interaction between the two shear layers. Inspired by the features of secondary instability, the flow control approach referred to as Spanwise Sinusoidal Perturbation (SSP) has been widely applied to control the nominally 2D wake flow of various two-dimensional bluff bodies, such as circular cylinders, square cylinders, airfoils and elliptic leading-edge bodies [12—17]. This approach usually involves periodic geometric modifications or suction and blowing on the leading or trailing edges of bluff bodies, which falls in the category of 3D forcing classified by Choi et al. [18]. The above-listed literatures suggest reduction in the drag force and suppression of the vortex shedding process by the SSP approach, especially when the perturbation wavelength is equal to the spanwise spacing of the dominant secondary instability. However, the optimal

wavelength is not common for various bluff bodies. This is due to the fact that the secondary wake insta-bility depends on the bluff body shape.

Besides the geometrical shape parameter, the flow Reynolds number affects the secondary instabilities significantly. This makes it difficult to determine the most effective perturbation wavelength for the SSP control. Within the laminar flow regime ($10 \leq \mathrm{Re} \leq 150$), Darekar and Sherwin [19] numerically investi-gated a square cylinder with spanwise sinusoidal waviness at the leading and trailing edges. Under the per-turbation wavelength of $5.6D$ (D is the leading edge height of the square cylinder) a maximum drag reduc-tion of 14% was obtained. This wavelength is very close to the spanwise spacing of the Mode A instability behind a square cylinder, as reported by the references [20, 21], for low Reynolds numbers ($\mathrm{Re} \leq 300$). In the turbulent regime ($\mathrm{Re} = 23\,500$) Dobre et al. [22] achieved 78% reduction of turbulence intensity using SSP at the leading edge of a square cylinder with a wavelength of $2.4D$. Following the experimental inlet condition of Dobre et al. [22], Antiohos et al. [16] performed large eddy simulations for a wavy square cyl-inder, in which up to 32% decrease in the mean drag and significant reduction in the lift fluctuations were achieved at a wavelength of $2.4D$. This wavelength is in accordance with the instability wavelength of Mode A reported by Dobre et al. [23] at the same Reynolds number. Similar results for a square cylinder having a sinusoidal front face can be found in the experimental work of Berman and Owen [24]. Never-theless, the greatest drag reduction was obtained with a perturbation wavelength of $5.6D$, which corre-sponds to the Mode A instability observed in the laminar flow regime. From above, we may infer that the optimum wavelength for SSP control is not universal and can vary with the change of the Reynolds num-ber. Therefore, it is interesting to examine whether the secondary instability observed for low Reynolds numbers can be served as a basis for the SSP control in the case of high Reynolds numbers, thus motivat-ing our work.

In the present study, the wavelength of Mode A instability observed at laminar flow regime is intro-duced to the leading edge of a square cylinder. To examine the effect of this wavelength in the turbulent regime, large eddy simulations were performed at the Reynolds number of $23\,500$. The results for the square cylinder are validated by the existing literature and PIV measurements. The detailed force charac-teristics and wake flow structures of the wavy square cylinder are captured and compared with a square cylinder. Comparisons are made in terms of aerodynamic force characteristics, mean- and instantaneous-flow fields, as well as time−frequency characteristics.

1. NUMERICAL AND EXPERIMENTAL METHODS

1.1. Numerical Solver

In the present study, the LES approach was adopted to solve the unsteady 3D incompressible flow over square and wavy-square cylinders using the FVM (Finite Volume Method) in ANSYS Fluent software. The 3D unsteady Navier−Stokes equations are solved by separating large-scale and small-scale velocity fields. The large-scale velocity fields are directly calculated, while the small-scale velocity fields are mod-eled by the subgrid-scale (SGS) model. The governing equations solved using LES are as follows:

$$\rho \frac{\partial \overline{u}_i}{\partial t} + \rho \overline{u}_j \frac{\partial \overline{u}_i}{\partial x_j} = -\frac{\partial \overline{p}}{\partial x_i} + \mu \frac{\partial^2 \overline{u}_i}{\partial x_j \partial x_j} - \frac{\partial \tau_{ij}}{\partial x_j}, \qquad (1.1)$$

$$\frac{\partial \overline{u}_i}{\partial x_i} = 0. \qquad (1.2)$$

Here, $\overline{u}_i$ and $\overline{p}$ are the filtered velocity and pressure, respectively, and τ_{ij} is the SGS stress tensor given by the expression $\tau_{ij} = \rho\overline{u_i u_j} - \rho\overline{u}_i\overline{u}_j$. In this study, the well-known Smagorinsky model is employed and the anisotropic part of the SGS stress tensor τ_{ij} is modeled as follows:

$$\tau_{ij} = -2\mu_t \overline{S}_{ij} + \frac{1}{3}\tau_{kk}\delta_{ij} \qquad (1.3)$$

where $\overline{S}_{ij}$ is the strain rate tensor. The SGS turbulent viscosity μ_t is written as

$$\mu_t \equiv \rho L_S^2 |\overline{S}| = \rho L_s \sqrt{2\overline{S}_{ij}\overline{S}_{ij}}, \qquad (1.4)$$

$$L_s = \min(\kappa\delta, C_s V^{1/3}), \qquad (1.5)$$

where L_s is the mixing length for the subgrid scales, κ is the von Kármán constant, C_s ($= 0.1$) is the Sma-gorinsky constant, δ is the distance to the closest wall, and V is the volume of the computational cell.
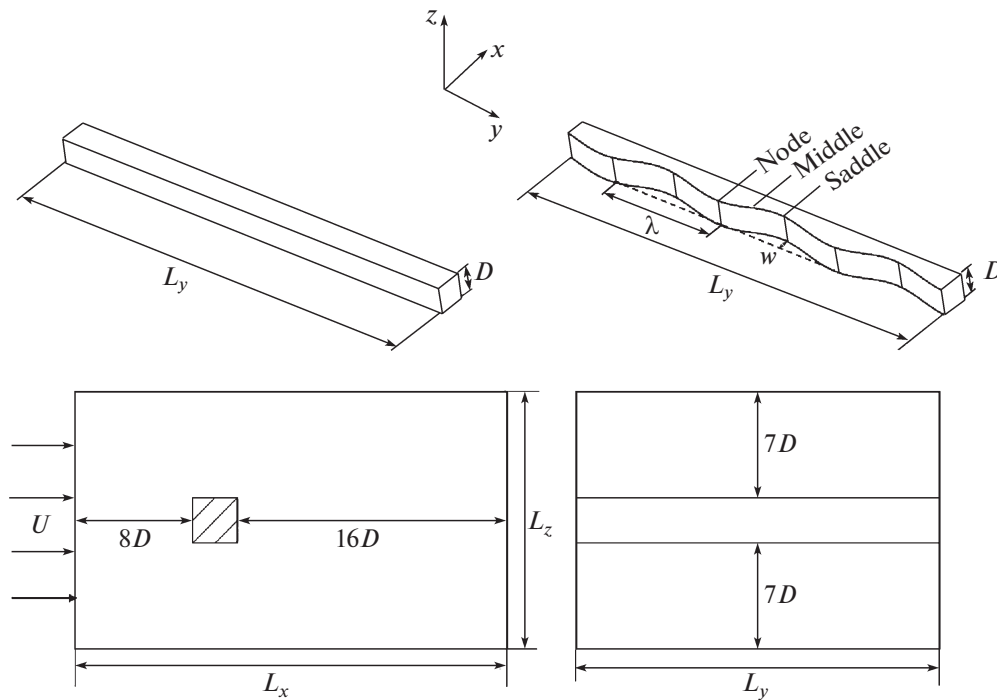
Fig. 1. Geometrical parameters and computational domain of the square and wavy-square cylinders.

In this study, a second-order implicit scheme is selected for the unsteady formulation and the pressure implicit splitting of operators (PISO) algorithm is adopted to solve the pressure-velocity coupling. The second-order and bounded central differencing schemes are applied to the spatial discretization of the pressure and momentum, respectively.

1.2. Computational Domain and Boundary Conditions

Figure 1 shows the geometrical parameters and computational domain of the square and wavy-square cylinders adopted in the present study. The square cylinder with a leading-edge height D and a spanwise length $L_y = 16.8D$ ($D = 20$ mm) was taken as the baseline case. For the wavy cylinder, the cross-section with maximum transverse edge is referred to as the node location and the cross-section with minimum transverse edge is referred to as the saddle location. The wavelength λ between two nodes is $5.6D$, and the sinusoidal amplitude $w = 0.45D$. A rectangular computational domain with the dimensions $L_x \times L_y \times L_z = 25D \times 16.8D \times 15D$ was chosen for numerical simulation. The inlet boundary is $8D$ upstream of the cylinder and the outlet boundary is located $16D$ downstream of the cylinder. The vertical height and the spanwise width of the computational domain are $15D$ and $16.8D$, respectively.

The velocity inlet boundary condition was assigned at a uniform velocity $U = 17.2$ m/s with turbulence intensity of 0.1%, resulting in the Reynolds number Re = 23 500 based on the leading-edge height of the computational models. The pressure outlet condition was used at the outlet of the computational domain. The symmetric boundary conditions were employed at the upper and lower boundaries in the vertical z direction. Periodic conditions were assigned at two side boundaries along the spanwise y direction. On the surfaces of the computational models, the no- slip boundary conditions were specified. Similar boundary conditions were used by Oka and Ishihara [25] for the turbulent flow over a square cylinder. The structural hexahedral grids for the square and wavy-square cylinders are shown in Fig. 2. As can be seen, nonuniform boundary-layer meshes were generated along the x- and z-directions, while uniform grids were set along the spanwise y direction with a resolution of $0.1D$. This grid resolution is fine enough to capture the unsteady behavior along the spanwise direction, as recommended by Mankbadi and Georgiadis [26]. In the xz plane, the distance between the nearest grids and the cylinder surfaces are set as $0.01D$ to ensure the dimensionless wall distance y^+ to be less than 1.

The computational mesh must be sufficiently fine to allow accurate prediction of instantaneous flow structures. The dependence of the numerical results on the gridpoint number for the flow around the
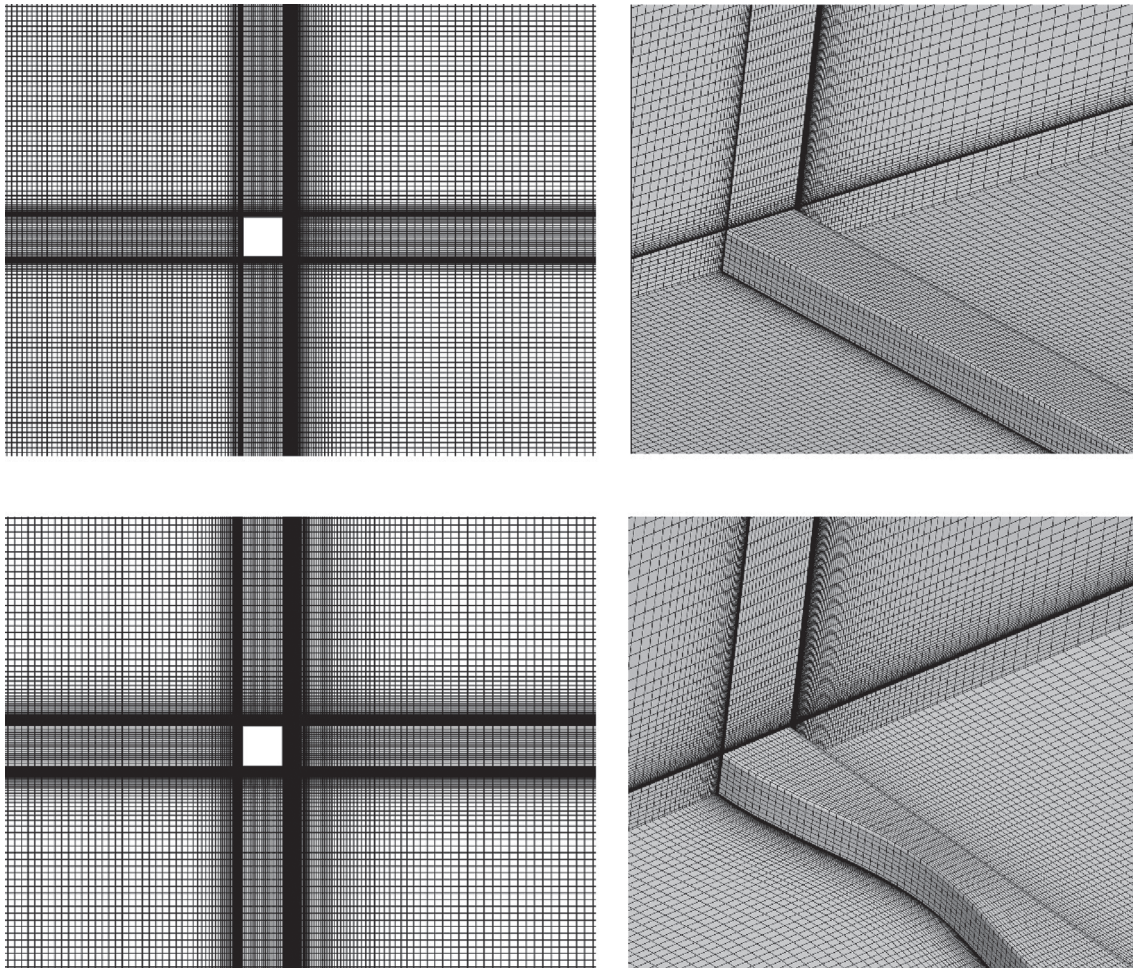
Fig. 2. Grid distributions of the square and wavy-square cylinders.

square cylinder was analyzed. The results involving the mean drag coefficient $\overline{C}_d$, the Strouhal number St, and the recirculation length Lr for four mesh configurations are shown in Table 1. With increase in the gridpoint number from $180 \times 168 \times 160$ (Case M1) to $260 \times 168 \times 220$ (Case M4), $\overline{C}_d$, St, and Lr vary about 3.1%, 5.2%, and 5.4%, respectively. When the gridpoint number increases from $240 \times 168 \times 200$ (Case M3) to $260 \times 168 \times 220$ (Case M4), the changes of $\overline{C}_d$, St, and Lr are not greater than 1%. To balance the computing cost and the result accuracy, the case M3 was chosen for numerical simulations. Additionally, it is noted that the recirculation length calculated from the present study is slightly smaller than the experimental result by Lyn et al. [27] and is greater than that in the numerical study by Murakami and Mochida [28]. This can be due to the differences in the inlet turbulence level, the aspect ratio, and the blockage ratio. The further validation of the present simulations was done by the comparison with the previously published results; it will be discussed in Section 2.

As the first step, the steady state computation was carried out and the results were used as the initial condition for unsteady flow computation. The non-dimensional time step $\Delta t^* = \Delta t\, U/D \approx 0.008$ was used for the LES simulations, leading to a Courant—Friedrichs—Levy (CFL) number lower than unity [29]. To obtain statistically converging results, 20 iterations were set in each time step and approximately 150 vortex shedding cycles were sampled for the cases of square- and wavy-square cylinders.

1.3. PIV-measurements

To validate the simulation results high-speed PIV measurements were performed using the circulating water channel of Rinoshika's Laboratory at the Yamagata University having 400 mm (width) × 300 mm (height) × 1000 mm (length) test section. The experimental models of the square- and wavy-square cyl-

Table 1. Tests of grid dependence for the smooth square cylinder

Cases	Grid size	$\bar{C}_d$	St	Lr/D
M1	180 × 168 × 160	2.31	0.127	1.22
M2	220 × 168 × 180	2.27	0.132	1.26
M3	240 × 168 × 200	2.25	0.134	1.28
M4	260 × 168 × 220	2.24	0.134	1.29

inders spanned the entire width of the test section and were placed in the water channel at the middle depth. The leading-edge height D of the experimental models is identical to the computational models. The spanwise length is equal to the water channel width, resulting in an aspect ratio of 20 with respect to the spanwise length of the experimental model. The measurements were carried out at a constant freestream velocity $U = 0.08$ m/s, which corresponds to the Reynolds number Re (UD/v) = 1553. The turbulence intensity was less than 0.5% of the freestream velocity.

The high-speed Photron FASTCAM SA3 camera having a resolution of 1024 × 1024 pixels was used to capture successive digital particle images in the streamwise and spanwise planes at a sampling frequency of 250 Hz. The compact laser generated by a 4 W continuous laser source was fitted with a cylindrical lens to produce a 1.5 mm light sheet along the measurement planes of the experimental models. Polystyrene particles with diameter of 10−25 μm were used as the PIV tracers in the flow loop. The instantaneous velocity vector fields were generated using the FFT-based cross-correlation technique between two successive particle images. The interrogation window size was 32 × 32 pixels with 50% overlap for each experimental condition. More details on the PIV measurements can be found in our previous study [30].

2. VALIDATION OF THE NUMERICAL RESULTS

To validate the numerical results the time histories of the z velocity component in the near wake region of the square cylinder were monitored to determine the power spectral density function (PSD) and the results were compared with the published experimental results. Figure 3 shows the PSD of the z velocity calculated at the location $x/D = 2$, $z/D = 2$, and $y = 0$, which is consistent with the analyzed configuration of W0 by Dorbe et al. [22]. The most prominent peak was observed around 118 Hz with a corresponding Strouhal number of 0.134 (St = fD/U) suggesting the associating vortex shedding frequency. A second peak in the PSD spectra was observed at St = 0.272, which is approximately twice of the first peak. As indicated by the dash line in Fig. 3, in the high frequency range the PSD spectra for the numerical results obey the −5/3 power law. These observations are in good agreement with the previous experimental and numerical studies [16, 22] of the wake flow of a square cylinder.

Table 2 provides the experimental and LES-predicted mean drag coefficient $\bar{C}_d$ and Strouhal number St for the case of the square cylinder. As can be seen, the of the recent case is very close to the experimental results by Bearman et al. [24] but it is slightly greater than from the works of Lyn et al. [26], Lin et al. [31], and Norberg [32] with a deviation no greater than 7.2%. As for the Strouhal number, it can be seen that the recent case is in good agreement with the listed literatures. To further validate the numerical results, the mean streamwise velocity of the wavy square cylinder obtained in the PIV experiment was compared with the LES results at the same inlet conditions. As shown in Fig. 4, the spatial distribution of the numerical results exhibits strong similarity with that of the experimental results characterized by an oval-like separation region behind the wavy square cylinder. Figure 5 presents the time-averaged streamwise velocity profiles for the numerical and experiment results, which were extracted at the locations $x/D = 2$ and 3 in the spanwise xy plane. Near the wavy square cylinder ($x/D = 2$) the LES underestimates slightly the magnitude of the streamwise velocity at the geometrical node positions (i.e., $y = 2.2$ and 7.8) compared to the experimental results. Further downstream in the wake ($x/D = 3$) overall good agreement with the experimental results is obtained.

3. RESULTS AND DISCUSSION

3.1. Drag and Lift Coefficients of the Square and Wavy-Square Cylinders

To investigate the impact of the wavy leading edge on the drag and lift of the square cylinder the time histories of the drag and lift coefficients are presented for the square and wavy-square cylinders. As shown in Fig. 6, the mean values of the drag coefficient for these two cases are 2.25 and 1.67, respectively. Up to
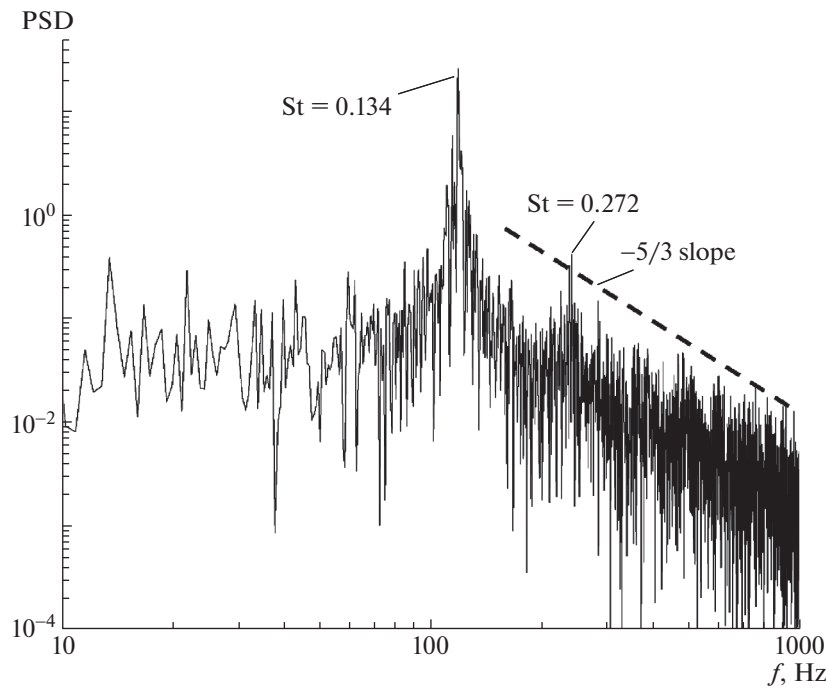
Fig. 3. PSD of the z velocity at the location ($x/D = 2$, $z/D = 2$, $y = 0$).

27% reduction of the mean drag acting on the wavy square cylinder is achieved, which is accompanied by a significant decrease in the amplitude of mean drag fluctuations. The RMS values of the drag coefficients for the square and wavy-square cylinders are 0.17 and 0.024, respectively. The lift coefficients of the square and wavy-square cylinders are plotted in Fig. 7. For the square cylinder periodical variation of the lift coefficient associated with the near wake vortex shedding is observed. However, the lift fluctuations of the wavy square cylinder do not show evident periodicity. In addition, a significant reduction in the lift coefficient for the wavy square cylinder is observed with a reduction of the RMS value up to 98%. This observation is quite similar with the numerical study by Antiohos et al. [16], in which an about 95% reduction was obtained for a square cylinder with a wavelength of 2.4D. The reduction of the drag and lift coefficients for the wavy square cylinder suggests the weakening of the vortex shedding process, which is helpful in engineering practice.

3.2. Time-Averaged Flow Fields

In the present study, the flow statistics were obtained over 120 vortex shedding cycles. Representative flow structures are presented in terms of streamline patterns and velocity and vorticity distributions. Figure 8 shows the time-averaged 3D streamlines and the vertical velocity distributions for the square and wavy-square cylinders. Here, the iso-contour indicates the time-averaged vertical velocity and the con-

Table 2. Mean drag coefficient and Strouhal number for the cases of the square cylinder

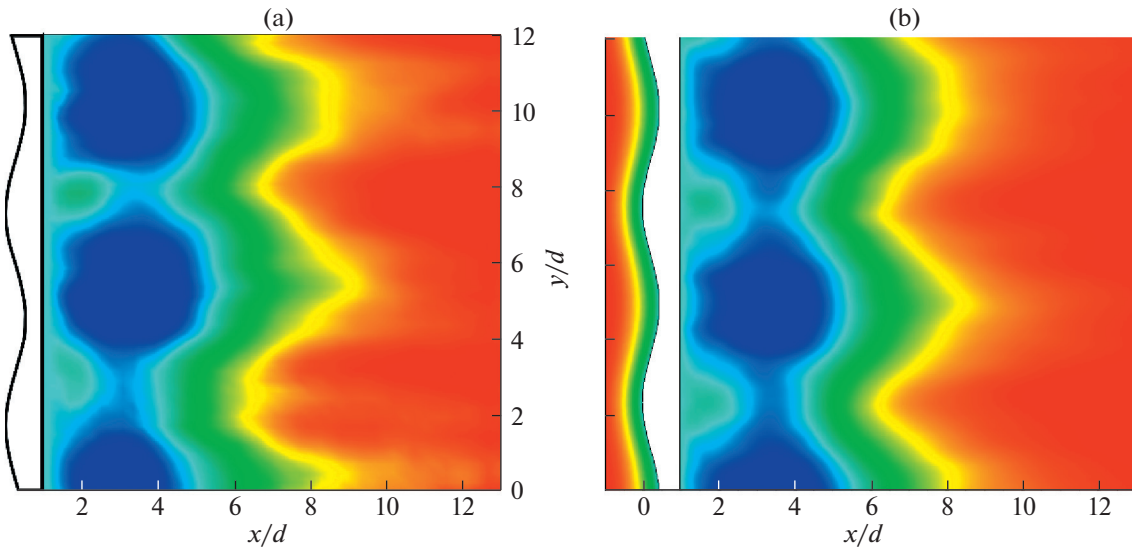| Case	Method	Re	$\bar{C}_d$	St
This case	LES	23 500	2.25	0.134
[16]	LES	23 500	2.346	0.139
[31]	LES	22 000	2.16	0.132
[24]	Experiment	22 000	2.24	0.130
[22]	Experiment	23 500	/	0.140
[32]	Experiment	22 000	2.10	0.130
[26]	Experiment	21 400	2.10	0.130

Fig. 4. Time-averaged streamwise velocity distribution at Reynolds number of 1553. (a) Experimental results and (b) numerical results.
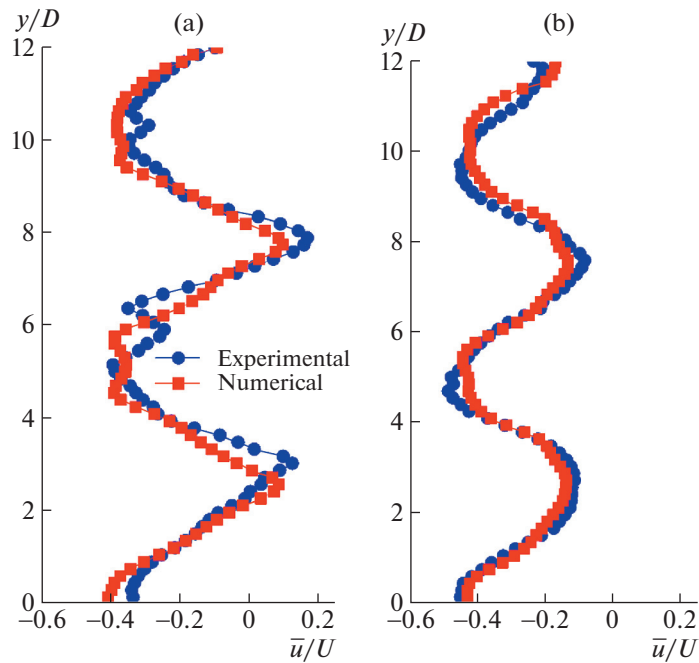

Fig. 5. Time-averaged streamwise velocity profiles at the locations (a) $x/D = 2$ and (b) 3.

tour plotted on the streamlines indicates the time-averaged streamwise velocity. As shown in Fig. 8a, a separation region characterized by vortex pairs stretched along the spanwise direction is clearly identified, exhibiting a predominantly two-dimensional nature. For the wavy square cylinder, as presented in Fig. 8b, the separation region is observed to be shifted further downstream with a sinusoidal variation, suggesting the three-dimensionality of the square cylinder wake. For both square and wavy-square cylinders, the time-averaged vertical velocity is antisymmetric with respect to the central spanwise plane, indicating the formation of separating shear layers. The iso-contour around the wavy square cylinder displays a strong spanwise variation, while the iso-contour of the square cylinder appears as a 2D region along the span. Outside the separation region, the vertical velocity component with the opposite sign is observed around
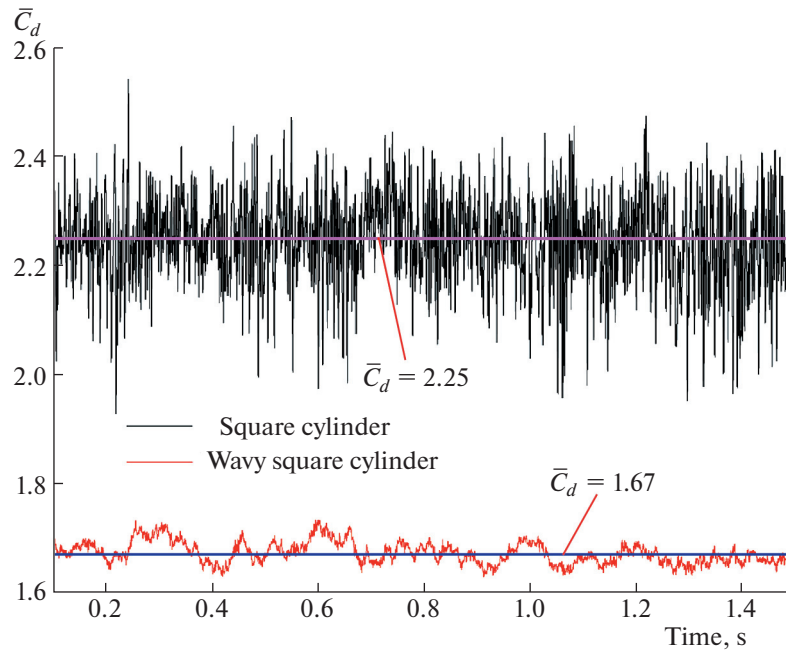
Fig. 6. Time histories of the drag coefficient for the square and wavy square cylinders.
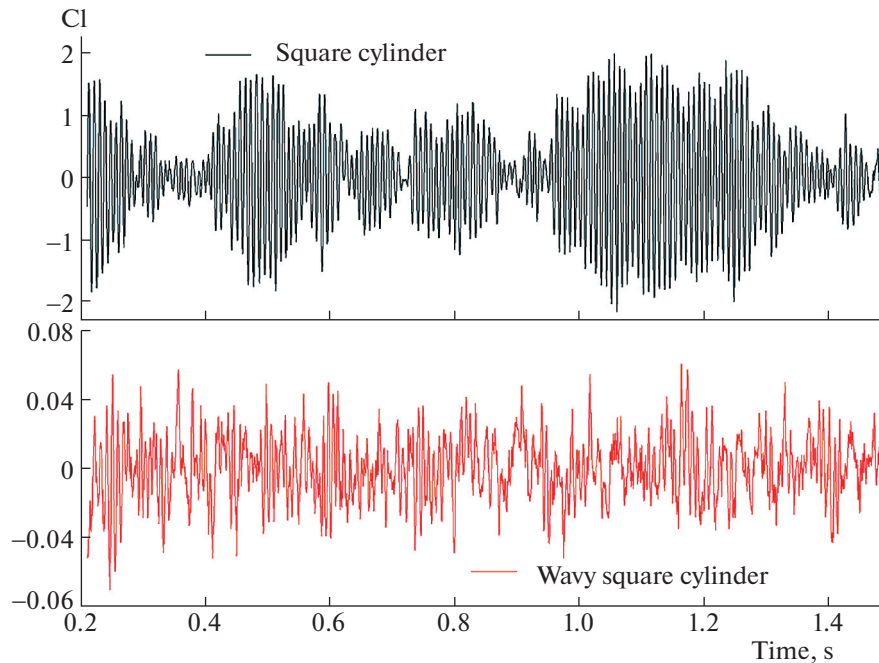

Fig. 7. Time histories of the lift coefficient for the square and wavy square cylinders.

the node position behind the wavy square cylinder. This implies that the flow entrainment between the main and wake flows is promoted behind the node position, resulting in a narrower and shorter reverse region, as indicated in Fig. 8b. Figure 9 shows the 3D separation region indicated by the iso-contours of time-averaged stream velocity with $\bar{u} = 0$ for the square- and wavy-square cylinder. The 2D streamlines are plotted on the middle spanwise plane. For the wavy square cylinder, as shown in Fig. 9b, a 3D oval-like separation region is clearly observed, and it extends to further downstream position compared with that of the square cylinder (Fig. 9a). Compared with the node position, the separation region formed
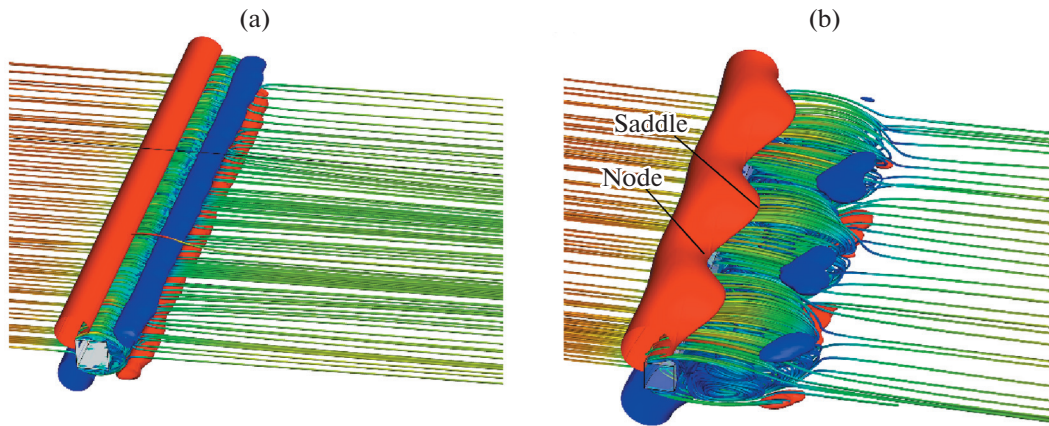
Fig. 8. Time-averaged 3D streamlines and vertical velocity distributions for the square and wavy-square cylinders; (a) square cylinder and (b) wavy-square cylinder.
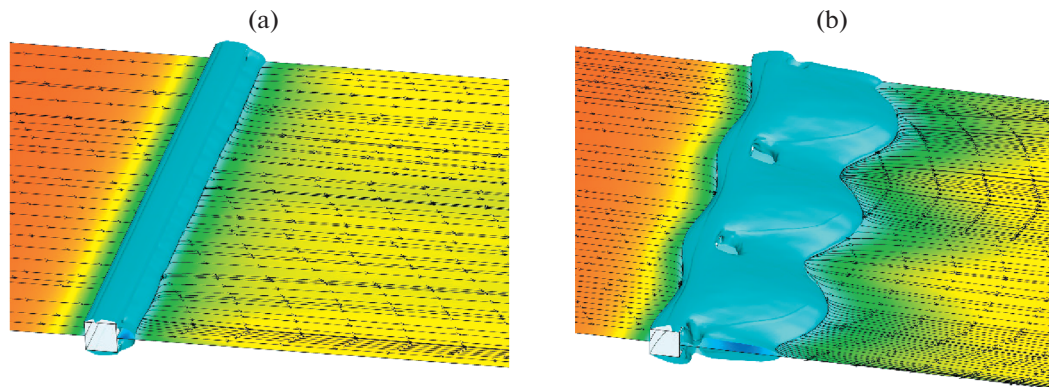

Fig. 9. Iso-contours of the time-averaged streamwise velocity and 2D streamlines for the square and wavy-square cylinders; (a) square cylinder and (b) wavy-square cylinder.

behind the saddle position is observed to be extended in both streamwise and vertical directions suggesting the three-dimensionality arising from the wavy leading edge. Furthermore, it is interesting to note that a region with a non-zero streamwise velocity distribution is observed behind the node position. This implies that flow separation around the node position occurs later than that around the saddle position. To further investigate the 3D flow structure induced by the wavy leading edge, iso-contours of the spanwise velocity components are presented in Fig. 10. Despite the averaging over 125 vortex shedding cycles, the spanwise velocity of the square cylinder (Fig. 10a) appears to be distributed randomly in the separation region. This can be attributed to the unsteadiness of small-scale turbulent fluctuations behind the square cylinder. For the wavy square cylinder, as shown in Fig. 10b, periodical repetitions of the spanwise velocity corresponding to the geometrical node and saddle positions are clearly identified, indicating that the additional spanwise motions are introduced by the wavy leading edge. As a result, high adjacent shear flow is generated between the geometric node and saddle position.

Figure 11 presents the 2D time-averaged streamline patterns for the square and wavy-square cylinders in the streamwise planes. For the square cylinder, the results were monitored at the central position along the span, while for the wavy square cylinder, as shown in Fig. 1, the monitoring planes were set along the node, middle, and saddle positions, respectively. In all the cases, symmetrical large-scale vortex pairs are observed with well-defined foci (F1, F2) and saddle points (S1). Obviously, the vortex formation length (distance from the center to the saddle point) for the case of the wavy square cylinder is much longer than that for the square cylinder. In the node plane of the wavy square cylinder (Fig. 11b), a clearly expressed saddle point (S2) is indicated by the streamline topology. This implies that the separation region is pushed further downstream from the node position, which is beneficial for drag force reduction. The delay of sep-
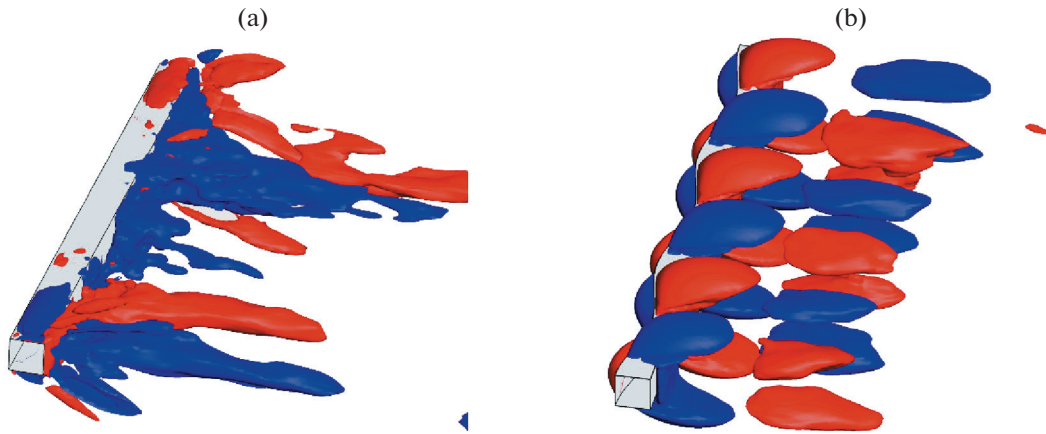
Fig. 10. Iso-contours of the time-averaged spanwise velocity component for the square and wavy-square cylinders; (a) square cylinder and (b) wavy-square cylinder.
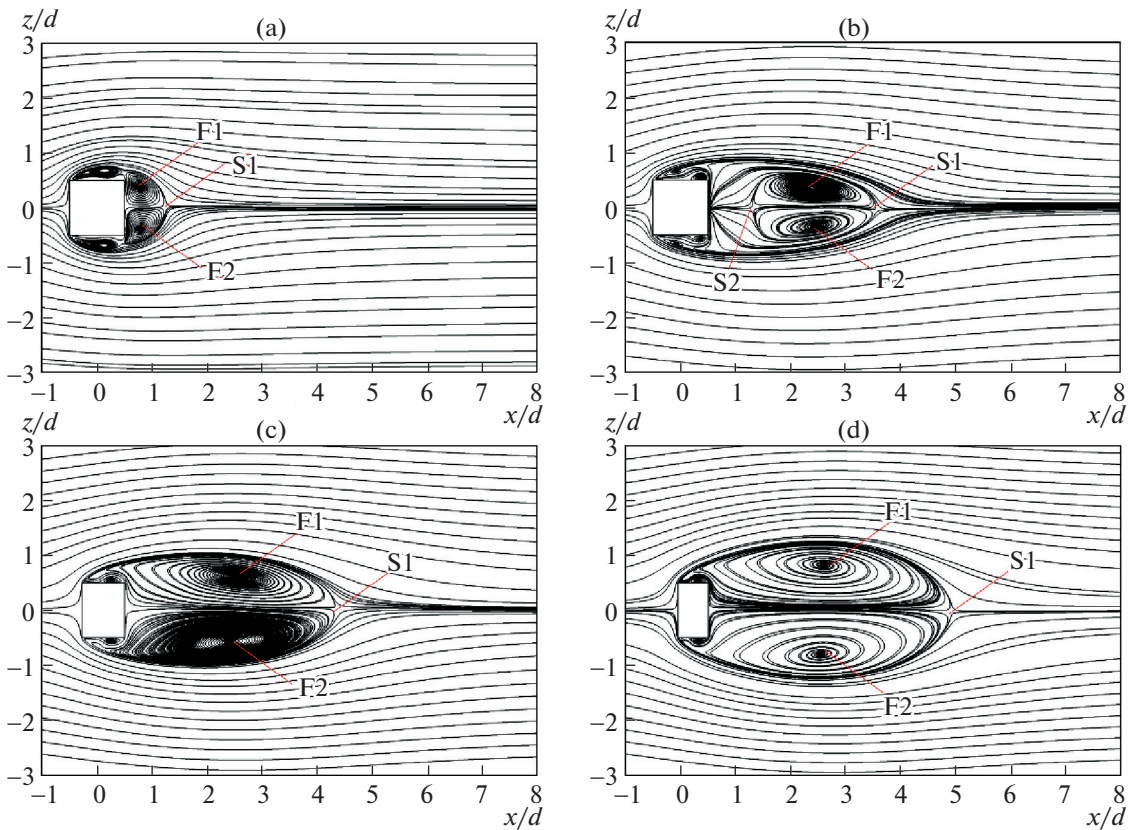

Fig. 11. 2D time-averaged streamline patterns for the square and wavy-square cylinders in the streamwise planes; (a) square cylinder, (b) node plane, (c) middle plane, and (d) saddle plane.

aration region can be attributed to the anti-symmetric spanwise velocity distribution around the node position, thanks to which the adjacent flow momentum is transferred inward the node plane. In addition, the change of the wake length and width is observed with the passage from the node to the saddle plane, thus further confirming the three-dimensionality in the wake of the wavy square cylinder.

To further investigate the flow structure induced the by the wavy leading edge, the time-averaged streamlines and vorticity contours for the wavy square cylinder are examined in the spanwise and cross-planes (xy and yz planes). As shown in Fig. 12, symmetrical vertical vortex pairs with opposite sense of
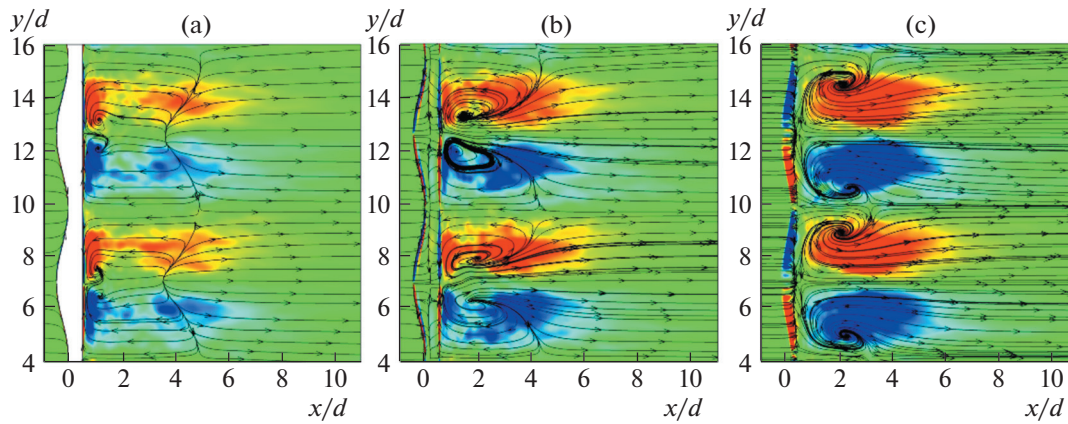
Fig. 12. 2D time-averaged streamline patterns and vertical vorticity contours for the wavy-square cylinder in the spanwise planes (a) $z/d = 0$, (b) 0.5, and (c) 0.6.

rotation are observed with respect to the node positions. In the central spanwise plane (Fig. 12a), the vortex pairs are formed immediately behind the rear surface of the wavy square cylinder and they help to delay the formation of separation region behind the node position. This observation is consistent with the time averaged streamline pattern presented in Fig. 11b. Apart from the central spanwise plane, the vortex pairs tend to expand toward the saddle location, resulting in a longer separation region around saddle the position, as indicated in Figs. 12b and 12c. Similar with the distribution of the vertical vortex structure presented in Fig. 12, counterrotating streamwise vortex pairs are observed in the cross planes (Fig. 13). These vortex pairs promote the generation of downwash flow behind the node position and upwash flow behind the saddle position. As a result, the wake width shrinks behind the node positions and expands in the region behind the saddle positions. The flow pattern displayed in the spanwise and cross planes implies that additional vertical and streamwise vortex structures are formed behind the wavy square cylinder, representing in a three-dimensional vortex along the span.

3.3. Instantaneous Flow Structures and Time-Frequency Characteristics

To capture the flow structures behind the square and wavy-square cylinders, typical 3D vortex structures are identified using the Q-criterion. Iso-surfaces with Q = 1200 are set to visualize the flow structures and are colored in accordance with the spanwise vorticity. For the square cylinder, as shown in Fig. 14a, the iso-surface exhibits a staggered pattern of the von Kàrmàn vortex street, which is primary two-dimensional along the span. For the wavy square cylinder (Fig. 14b) the staggered pattern is obviously weakened, indicating the suppression of the vortex shedding process. Furthermore, it should be noted that wavy distributed spanwise vortices are discernible at fixed positions along the spanwise direction. Compared with the square cylinder, these vortices are more stable and promote the dislocation of the large-scale vortex preventing the shear layer from rolling up into a vortex street. This can be inferred as a reason for longer vortex formation length behind the wavy square cylinder. Figure 15 shows the instantaneous vorticity and streamline patterns for the square and wavy square cylinders in the streamwise planes. For the case of the square cylinder (Fig. 15a), the lower shear layer rolls up immediately from backside of square cylinder, while the upper shear layer begins to move in the reverse direction. As a result, alternatively distributed Kármán vortex pairs with opposite sense of rotation are generated in the upper and lower shear layers. This observation suggests an asymmetric shedding mode behind the square cylinder, which is consistent with the classical Kármán vortex shedding process. For the wavy square cylinder (Figs. 15b–15d), the separated shear layer is observed to be symmetric about the wake center line. Within the shear layer, small-scale vortex pairs resulting from the wavy leading edge tend to shed simultaneously behind the wavy square cylinder, indicating a symmetric shedding mode in the near wake region. However, the symmetrical vortex shedding disappears further downstream (i.e., at $x = 3$ in the middle plane, Fig. 15c), where a large-scale vortex begins to roll up or down into the vortex street. These vortex pairs play a role in preventing the upper and lower shear layers from interacting with each other in the near wake region. Such a symmetric near-wake vortex structure is considered to be associated with the reduction in the drag and lift coefficients of the wavy square cylinder. Furthermore, it is worthy to note that the wake shedding processes are not synchronous in the node and saddle planes, implying the dislocation of the vortex structure.
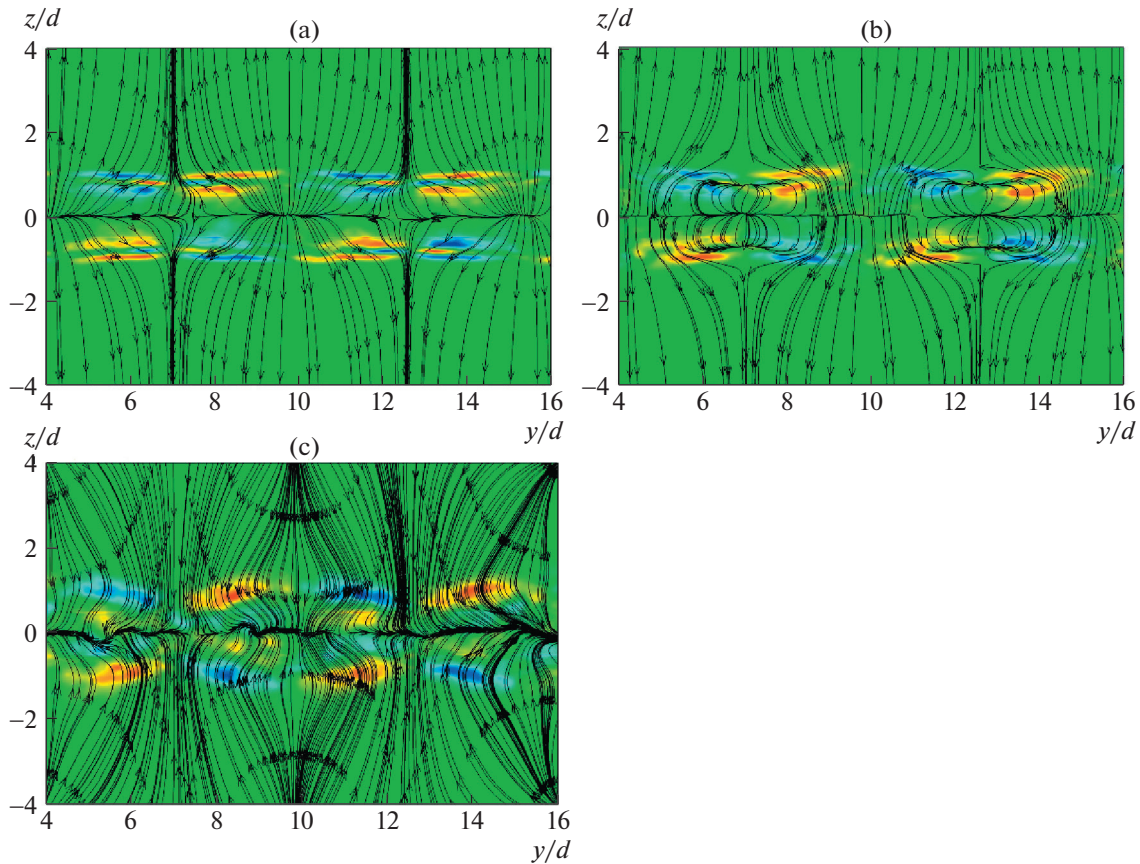
Fig. 13. 2D time-averaged streamline patterns and streamwise vorticity contours for the wavy-square cylinder in the cross planes (a) $x/d = 1$, (b) 2, and (c) 3.
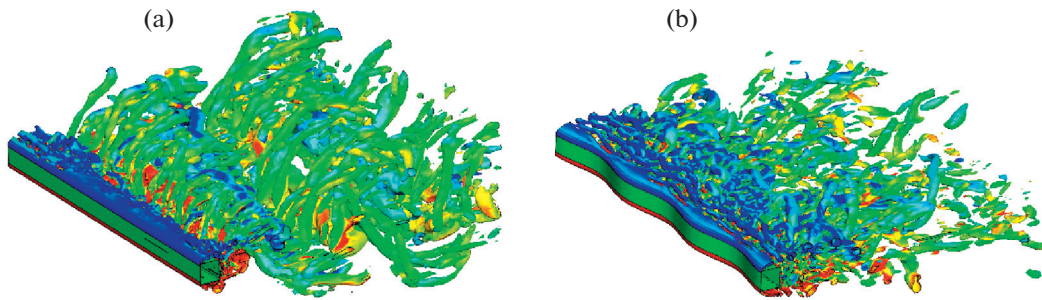

Fig. 14. Typical 3D vortex structures for the square and wavy-square cylinders identified by the Q-criterion; (a) square cylinder and (b) wavy-square cylinder.

To investigate the vortex shedding behavior behind the square and wavy-square cylinders, the continuous wavelet transform (CWT) using the Mexican Hat as the mother wavelet is adopted to reveal the temporal and spectral information at representative points in streamwise planes. The results are visualized by mapping the wavelet coefficients in time−frequency planes. Figure 16 shows the coefficients of CWT at the representative points ($x/D = 0.8$, $z/D = 4.3$, square cylinder; $x/D = 1.1$, $z/D = 4.4$, node plane; $x/D = 2.0$, $z/D = 4.5$, middle plane; and $x/D = 2.5$, $z/D = 4.7$, saddle plane), which are located approximately on the vortex path. Below the figure, the corresponding time history of the fluctuating velocity at each point is presented. As shown in Fig. 16a, alternative positive and negative peaks corresponding to the quasi-periodical variation of the fluctuating velocity appear at around 120 Hz, which is consistent with the result of PSD presented in Fig. 3. Evidently, this frequency is associated with the large-scale vortex
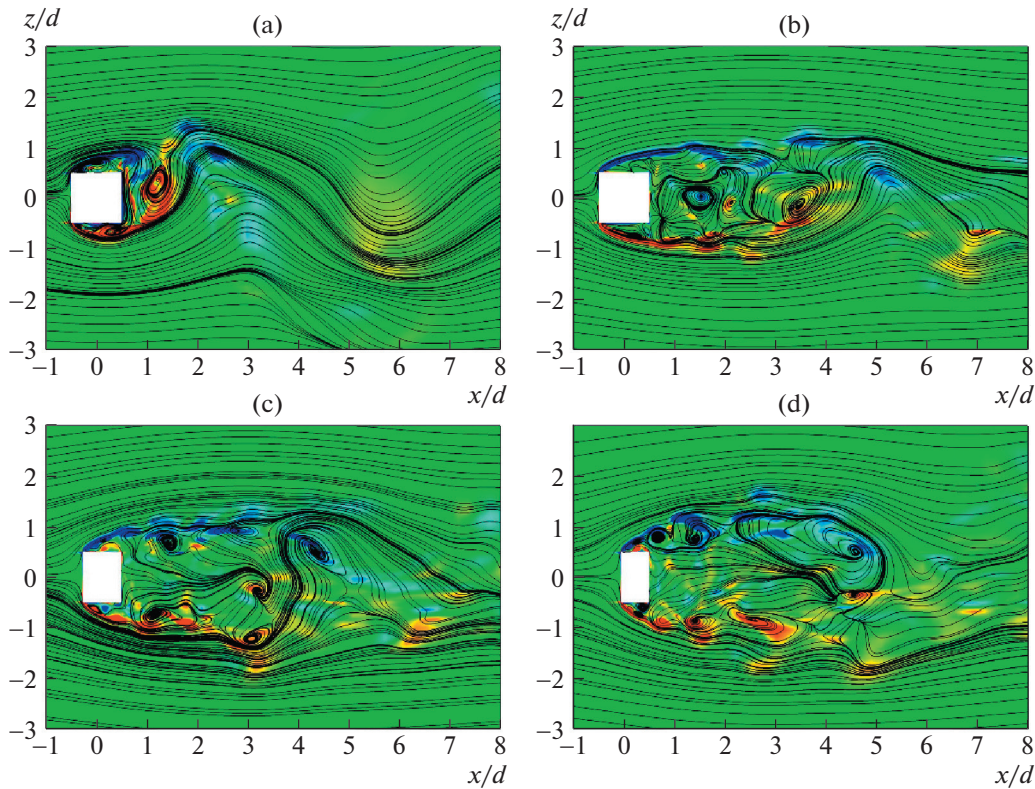
Fig. 15. Instantaneous vorticity and streamline patterns for the square and wavy-square cylinders in the streamwise planes; (a) square cylinder, (b) node plane, (c) middle plane, and (d) saddle plane.

shedding behind the square cylinder. In the range of relatively high frequencies ($f > 200$ Hz) small streaks are observed between positive and negative peaks, indicating the existence of small-scale flow structures. Compared with the case of the square cylinder, the time histories for the wavy square cylinder (Figs. 16b–16d) do not exhibit evident periodicity, suggesting the weakening of regular flow oscillations by the wavy leading edge. Concerning the time-frequency distributions, a decrease in the peak frequency can be observed for the cases of the wavy square cylinder, indicating a relatively steady wake flow. This can be attributed to the vortex dislocation behind the wavy square cylinder. In the range of relatively high frequencies, the small streaks appear more frequently than those in the case of the square cylinder, indicating that small-scale fluctuations are enhanced by the wavy leading edge. This can be due to the symmetric near-wake vortex which promotes the breakdown of the large-scale vortex into small-scale vortex structures.

SUMMARY

Three-dimensional flow structures around square and wavy-square cylinders are investigated using the LES approach at the Reynolds number of 23 500. The results are validated against the existing literature data and PIV measurement. Comparisons between the square and wavy-square cylinders are performed in terms of the drag force characteristics and the mean and instantaneous flow fields, as well as using the time-frequency analysis. The numerical results suggest that the perturbation wavelength of $5.6D$ changes the wake flow structure significantly and it can be served as the fundamental parameter for the SSP control in a turbulent flow regime. The main results are summarized as follows:

1. The wavy leading edge can give rise to remarkable reductions in the drag and lift forces on the square cylinder. Up to 27% and 98% reduction in the mean drag and the lift fluctuations are achieved, respectively.

2. A 3D oval-like separation region is formed behind the wavy square cylinder with a strong spanwise variation, suggesting the three-dimensionality of the wake flow structure. The flow separation around the node position occurs later than that around the saddle position, which can be attributed to the anti-sym-
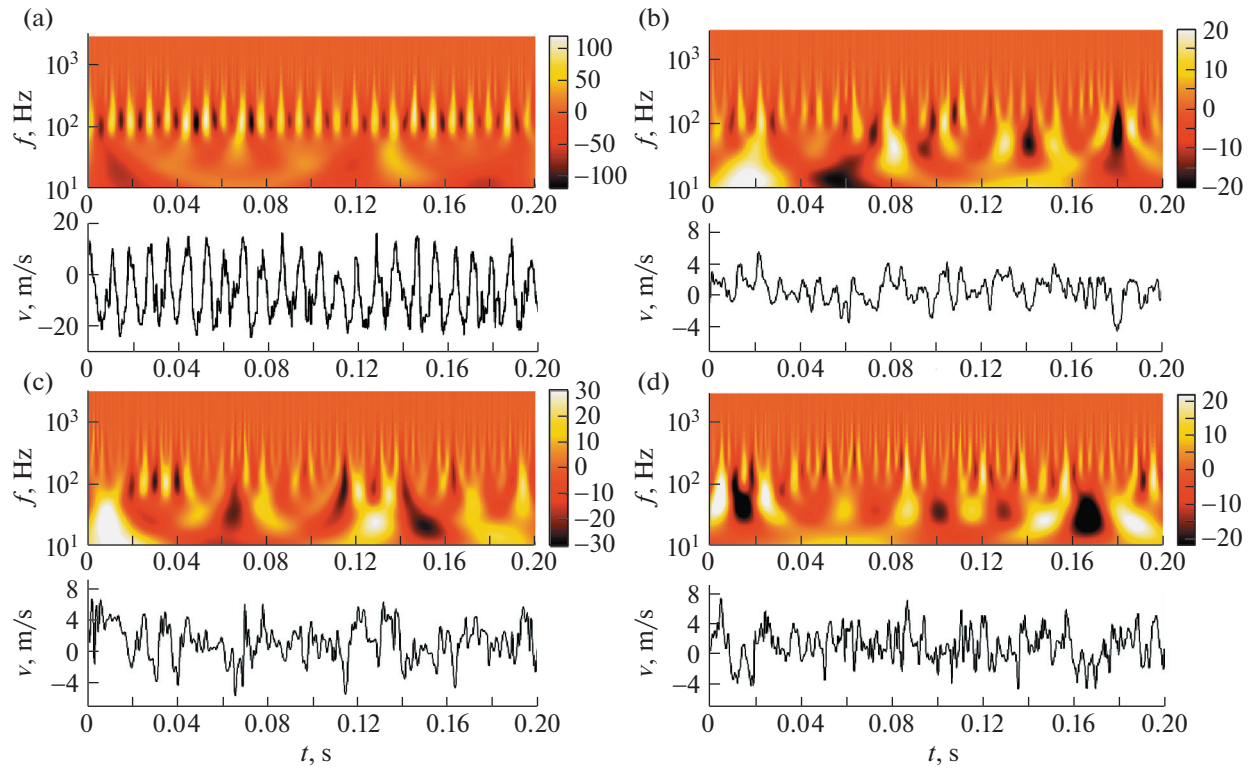
Fig. 16. Time-frequency distributions for the square and wavy-square cylinders at representative points (a) $x/D = 0.8$, $z/D = 4.3$, square cylinder; (b) $x/D = 1.1$, $z/D = 4.4$, node plane; (c) $x/D = 2.0$, $z/D = 4.5$, middle plane; and (d) $x/D = 2.5$, $z/D = 4.7$, saddle plane.

metric spanwise velocity distribution around the node position, by means of which the adjacent flow momentum is transferred inward the node plane.

3. Counterrotating streamwise and vertical vortex pairs are observed in the cross planes and the spanwise planes, respectively. These vortex pairs lead to the change in separation region width and length.

4. The 3D instantaneous vortex structures behind the wavy square cylinder are more stable and promote the dislocation of the large-scale vortex thus preventing the shear layer from rolling up into a vortex street. The 2D flow patterns of the wavy square cylinder suggest the symmetric shedding mode in the near wake region. This symmetric near wake vortex structure plays a role in preventing the upper and lower shear layers from interacting with each other in the near-wake region.

5. In the low frequency range a reduction in the dominating vortex shedding frequency is observed for the case of the wavy square cylinder, indicating a relatively steady wake flow. This can be attributed to the vortex dislocation behind the wavy square cylinder. In the high frequency range small streaks associated with small-scale fluctuations are enhanced by the wavy leading edge. This can be due to the symmetric near-wake vortex which promotes the breakdown of the large-scale vortex into small-scale vortex structures.

CONFLICT OF INTEREST

The authors declare that they have no conflicts of interest.

REFERENCES

1. Chen, Y.J. and Shao, C.P., Suppression of vortex shedding from a rectangular cylinder at low Reynolds numbers, *J. Fluids Struct.*, 2013, vol. 43, no. 7, pp. 15−27.
2. Chauhan, M.K., Dutta, S., and Gandhi, B.K., Wake flow modification behind a square cylinder using control rods, *J. Wind Eng. Ind. Aerodyn.*, 2019, vol. 184, pp. 342−361.
3. Kim, J. and Choi, H., Distributed forcing of flow over a circular cylinder, *Phys. Fluids,* 2005, vol. 17, no. 3, pp. 35−35.
4. Rathakrishnan, E., Effect of splitter plate on bluff body drag, *AIAA J.*, 1999, vol. 37, no. 9, pp. 1125−1126.
5. Lam, K. and Lin, Y.F., Effect of wavelength and amplitude of a wavy cylinder in cross flow at low Reynolds numbers, *J. Fluid Mech.,* 2009, vol. 620, pp. 195−220.
6. Williamson, C.H.K., Vortex dynamics in cylinder wake, *Annu. Rev. Fluid Mech.*, 1996, vol. 28, pp. 477−539.
7. Robichaux, J., Balachandar, S., and Vanka, S.P., Three-dimensional Floquet instability of the wake of square cylinder, *Phys. Fluids,* 1999, vol. 11, no. 3, pp. 560−578.
8. Naghib-Lahouti, A., Lavoie, P., and Hangan, H., Wake instabilities of a blunt trailing edge profiled body at intermediate Reynolds numbers, *Exp. Fluids*, 2014, vol. 55, no. 7, p. 1779.
9. Luo, S.C., Tong, X.H., and Khoo, B.C., Transition phenomena in the wake of a square cylinder, *J. Fluids Struct.*, 2007, vol. 23, pp. 227−248.
10. Ryan, K., Thompson, M.C., and Hourigan, K., Three-dimensional transition in the wake of elongated bluff bodies, *J. Fluid Mech.,* 2005, vol. 538, pp. 1−29.
11. El-Gammal, M. and Hangan, H., Three-dimensional wake dynamics of a blunt and divergent trailing edge airfoil, *Exp. Fluids*, 2008, vol. 44, no. 5, pp. 705−717.
12. Lam, K., Lin, Y.F., Zou, L., and Liu, Y., Investigation of turbulent flow past a yawed wavy cylinder, *J. Fluids Struct.*, 2010, vol. 26, nos. 7−8, pp. 1078−1097.
13. Zhang, W., Daichin, and Sang, J.L., PIV measurements of the near-wake behind a sinusoidal cylinder, *Exp. Fluids*, 2005, vol. 38, no. 6, pp. 824−832.
14. New, T.H., Shi, S., and Liu, Y., On the flow behaviour of confined finite-length wavy cylinders, *J. Fluids Struct.*, 2015, vol. 54, pp. 281−296.
15. Naghib-Lahouti, A., Doddipatla, L.S., and Hangan, H., Secondary wake instabilities of a blunt trailing edge profiled body as a basis for flow control, *Exp. Fluids*, 2012, vol. 52, no. 6, pp. 1547−1566.
16. Antiohos, A.A. and Thorpe, G.R., Effect of aspect ratio of a spanwise sinusoidal profile on the control of turbulent flows around bluff bodies, *J. Wind Eng. Ind. Aerodyn.,* 2015, vol. 145, pp. 237−251.
17. Lam, K., Lin, Y.F., Zou, L., and Liu, Y., Numerical study of flow patterns and force characteristics for square and rectangular cylinders with wavy surfaces, *J. Fluids Struct.,* 2012, vol. 28, pp. 359−377.
18. Choi, H., Jeon, W.P., and Kim, J., Control of flow over a bluff body, *Annu. Rev. Fluid Mech.*, 2008, vol. 40, pp. 113−139.
19. Darekar, R.M. and Sherwin, S.J., "Flow past a square-section cylinder with wavy stagnation face, *J. Fluid Mech.,* 2001, vol. 426, pp. 263−295.
20. Sheard, G.J., Fitzgerald, M.J., and Ryan, K., Cylinders with square cross-section: wake instabilities with incidence angle variation, *J. Fluid Mech.*, 2009, vol. 630, pp. 43−69.
21. Tong, X.H., Luo, S.C., and Khoo, B.C., Transition phenomena in the wake of an inclined square cylinder, *J. Fluids Struct.*, 2008, vol. 24, pp. 994−1005.
22. Dobre, A., Hangan, H., and Vickery, B.J., Wake control based on spanwise sinusoidal perturbation, *AIAA J.*, 2006, vol. 44, no. 3, pp. 485−492.
23. Dobre, A. and Hangan, H., Investigation of the three-dimensional intermediate wake topology for a square cylinder at high Reynolds number, *Exp. Fluids*, 2004, vol. 37, no. 4, pp. 518−530.
24. Bearman, P.W. and Owen, J.C., Reduction of bluff body drag and suppression of vortex shedding by the introduction of wavy separation lines, *J. Fluids Struct.,* 1998, vol. 12, pp. 123−130.
25. Oka, S. and Ishihara, T., Numerical study of aerodynamic characteristics of a square prism in a uniform flow, *J. Wind Eng. Ind. Aerodyn.*, 2009, vol. 97, pp. 548−559.
26. Mankbadi, M.R. and Georgiadis, N.J., Examination of parameters affecting large-eddy simulations of flow past a square cylinder, *AIAA J.*, 2015, vol. 53, no. 6, pp. 1706−1712.
27. Lyn, D.A., Einav, S., Rodi, W., and Park, J.H., A laser-Doppler velocimetry study of ensemble-averaged characteristics of the turbulent near wake of a square cylinder, *J. Fluid Mech.*, 1995, vol. 304, pp. 285−319.
28. Murakami, S. and Mochida, A., On turbulent vortex shedding flow past 2d square cylinder predicted by CFD, *J. Wind Eng. Ind. Aerodyn.*, 1995, vol. 54−55, pp. 192−211.
29. Lin, Y.F., Bai, H.L., Alam, M.M., Zhang, W.G., and Lam, K., Effects of large spanwise wavelength on the wake of a sinusoidal wavy cylinder, *J. Fluids Struct.*, 2016, vol. 61, p. 392.
30. Zheng, Y., Rinoshika, H., Zhang, D., and Rinoshika, A., Analyses on flow structures behind a wavy square cylinder based on continuous wavelet transform and dynamic mode decomposition, *Ocean Eng.,* 2020, vol. 206, p. 108117.
31. Lin, Y.F., Bai, H.L., and Alam, M.M., The turbulent wake of a square prism with wavy faces, *Wind. Struct. An Int. J.*, 2016, vol. 23, no. 2, pp. 127−142.
32. Norberg, C., Flow around rectangular cylinders: Pressure forces and wake frequencies, *J. Wind Eng. Ind. Aerodyn.,* 1993, vol. 49, nos. 1−3, pp. 187−196.